Salcedo-Abraira, P.; Santiago-Portillo, A.; Atienzar Corvillo, PE.; Bordet, P.; Salles, F.; Guillou, N.; Elkaim, E.... (2019). A highly conductive nanostructured PEDOT polymer confined into the mesoporous MIL-100(Fe). Dalton Transactions. 48(26):9807-9817. https://doi.org/10.1039/c9dt00917e

Dalton Transactions

ARTICLE

Highly conductive nanostructured PEDOT polymer confined into the mesoporous MIL-100(Fe) †

Received 00th January 20xx,
Accepted 00th January 20xx

DOI: 10.1039/x0xx00000x

www.rsc.org/

Pablo Salcedo-Abraira ,[a‡] Andrea Santiago-Portillo,[b‡] Pedro Atienzar,[b] Pierre Bordet,[c] Fabrice Salles,[d] Nathalie Guillou,[e] Erik Elkaim,[f] Hermenegildo Garcia,[b] Sergio Navalon,[b]* Patricia Horcajada[a]*

Despite the higher efficiency, larger color range and faster stimulus response of polymeric electrochromic materials, their poor cyclability strongly hampers their application in optoelectronics. As an original strategy to stabilize and further nanostructure the polymer, herein the efficient encapsulation and *in situ* polymerization inside the high porosity of Metal-Organic Frameworks (MOFs) is reported. In particular, the successful accommodation of poly(3,4-ethylendioxythiophene) (PEDOT) and its partially oxidized polarons inside the mesoporosity of the nontoxic iron trimesate MIL-100(Fe) is convincingly proved by a large panel of experimental techniques. Remarkably, the polymer MOF interaction occurring for entrapped PEDOT within the pores (deeply assessed by experimental and simulation methods) might be responsible for the enhanced electrical conductivity of the resulting PEDOT@MIL-100(Fe) composite when compared to the insulating MIL-100(Fe) and the conductive free PEDOT. Further, it was possible to observe the electrochromic properties of the PEDOT@MIL-100(Fe) composite, achieving an improved stability and good cyclability as consequence of the effective protection by the MOF matrix.

Introduction.

Electrochromic materials, able to change their optical properties when an electric current is applied[1], are very interesting due to their use in a wide range of cutting-edge technological areas, such as light controllers or optical shutters (*e.g.* mirrors, smart windows, sunglasses). Among them, transition metal oxides,[2–4] Prussian blue analogues[5] and organic conducting polymers[6,7] have attracted considerable attention. Despite their limitations concerning the color tailorability and brightness, the most commonly used smart materials are the inorganic ones (*e.g.* mainly WO_3, as well as TiO_2 and V_2O_5) due to their excellent stability and cyclability. In contrast, polymers have higher color intensity, larger variability in the choice of the color range and faster stimulus response, as well as other advantages (*e.g.* electrical conductivity, easy chemical tunability, low-cost and facile processability).[8] Cyclability of organic conducting polymers is, however, unsatisfactory as consequence of the severe stability issues, which hampers their real application in optoelectronics. This is a consequence of their structural disordered nature and the important volumetric changes occurred during operation of the devices.

Encapsulation within the cavities of porous insulating materials (*e.g.* zeolites or mesoporous silica) has been widely proposed as a general strategy to stabilize conducting polymers (CPs). However, this approach present important drawbacks such as diffusional limitation, inefficient polymerization and/or low chemical and structural versatility.[9–11] As an alternative, the encapsulation of CPs in highly porous hybrid host matrices, like Metal-Organic Frameworks (MOFs), has recently emerged as a promising method to achieve efficient CPs loadings and adequate polymerization.[12] MOFs, built up from inorganic subunits (atoms, clusters, chains,…) and organic polytopic linkers (phosphonates, carboxylates, azolates…), combine a very high regular porosity (pore volume up to 2 $cm^3 \cdot g^{-1}$; specific BET surface area = 7000 $m^2 \cdot g^{-1}$; pore diameter = 3-98 Å)[13–15] with an easily tunable composition and topology. Due to their outstanding properties, MOFs have been extensively proposed in economically key applications (fluid separation and capture, sensing, heterogeneous catalysis, energy and biomedicine, among others) .[16–18] However, the possibility to apply MOFs in optoelectronics, generally requiring conductive materials, has been almost unexplored, probably as a consequence of the poor electronic conduction of most MOFs. Thus, to the best of our knowledge, only six MOF structures have been recently reported exhibiting electrochromic properties with a modest

[a] Advanced Porous Materials Unit, IMDEA Energy, Avda. Ramón y Cajal 3, 28935 Móstoles-Madrid, Spain.
[b] Department of Chemistry and Instituto de Tecnología Química, Consejo Superior de Investigaciones Científicas-Universitat Politècnica de València, C/Camino de Vera, s/n, 46022, Valencia, Spain.
[c] Institute NEEL CNRS/UGA, 25 rue des Martyrs, Grenoble cedex 9, France.
[d] Institut Charles Gerhardt Montpellier, UMR 5253 CNRS UM ENSCM, Université Montpellier, Place E. Bataillon, 34095 Montpellier Cedex 05, France.
[e] Institut Lavoisier de Versailles, UMR CNRS 8180, Université de Versailles St-Quentin en Yvelines, Université Paris Saclav, 45 Av. des Etats-Unis, 78035 Versailles, France.
[f] CRISTAL Beamline, Synchrotron Soleil, L'orme des Merisiers, Saint-Aubin, BP 48, 91192 Gif-sur-Yvette Cedex, France

‡ These authors contributed to this manuscript equally.
† Electronic Supplementary Information (ESI) available: [details of any supplementary information available should be included here]. See DOI: 10.1039/x0xx00000x

cyclability.[19–23] *De novo* synthesis of new conductive MOFs is however time-consuming and complex, requiring sophisticated non-commercial ligands and tedious optimization of the synthetic parameters.

In this context, the entrapment of a CP within the voids of a highly stable known MOF will be here presented, characterizing the electrochromic properties of the resulting composite. Although scarcely explored and with different aims, the encapsulation of some CPs have been already reported within a few low density MOF architectures (MIL-101(Cr), HKUST-1, DUT-4, DUT-5, $[La(BTB)]_n$, $Zn_2(1,4\text{-ndc})_2(dabco)$).[24–29] As a general observation, more stable materials with improved properties (*e.g.* electrical conductivity, optical, ion diffusion, sensing) are generally achieved as result of encapsulation.

The well-known CP poly(3,4-ethylendioxythiophene) (PEDOT) has been successfully encapsulated within the pores of the non-toxic iron(III) trimesate MIL-100(Fe) (MIL stands for Material of Institut Lavoisier) using a two-step protocol: first, adsorbing the monomer and then, by its *in situ* oxidative polymerization within the MOF matrix. PEDOT was selected, as an extensively studied active material, due to its excellent properties in electrochromic devices.[30,31] On the other hand, the benchmarked MIL-100(Fe) solid was chosen as host matrix owing to its features: i) remarkable porosity with an adequate pore size, compatible with the monomer dimensions, ii) high chemical and thermal stability, iii) environmentally friendly character, iv) green and scalable synthesis, v) presence of coordinatively unsaturated metal sites (CUS) with a Lewis acid character and vi) a reversible redox behavior.[32–35] The successful accommodation of PEDOT and its partially oxidized polarons within the MIL-100(Fe) pores was thus convincingly supported by a combination of different techniques, including powder X-ray diffraction (PXRD), thermogravimetric analysis (TGA), Fourier transform infrared spectroscopy (FTIR), N_2 sorption measurements, scanning electron microscopy coupled with an energy dispersive X-ray spectrometer (SEM-EDX), UV-Vis spectroscopy, electron paramagnetic resonance (EPR) and ζ-potential. Further, PEDOT@MIL-100(Fe) was characterized by a combination of experimental (FTIR and pair distribution function-PDF analysis using high resolution synchrotron data) and molecular simulations (Grand Canonical Monte Carlo-GCMC and Density Functional Theory-DFT) in order to elucidate the polymer conformation inside the MOF. Finally, the electrochromic properties of the resulting PEDOT@MIL-100(Fe) composite were evaluated with respect to its potential as electrochromic devices.

Results and discussion.

The conducting polymer PEDOT was successfully entrapped within the MIL-100(Fe) mesopores using a simple and efficient two-step process. Initially, the EDOT monomer was adsorbed by suspending the previously dehydrated MOF in a concentrated EDOT solution. Subsequently, encapsulated EDOT was submitted to *in situ* oxidative polymerization within the MOF pores using an acetonitrile solution of anhydrous $FeCl_3$ (see experimental section; Figure 1). First, the EDOT encapsulation process was optimized by investigating the influence of the impregnation solvent (*i.e.* acetonitrile and hexane) and EDOT:MOF wt. ratio (*i.e.* 0.45:1, 0.9:1 and 1.8:1). Using a 90% (w/w) EDOT:MIL-100(Fe) ratio in hexane or acetonitrile and a subsequent polymerization with $FeCl_3$,[36] the amount of entrapped PEDOT was 60 and 4 wt.% (based in the dry MIL-100(Fe)), respectively (Figure S1 and Table 1). The much lower PEDOT insertion in acetonitrile might be related with the competitive adsorption of this polar solvent within the MOF. Indeed, it is well-established that small polar molecules such as H_2O, CH_3CN or dimethylformamide (DMF) can strongly interact with the iron CUS of MIL-100(Fe) acting as Lewis centers. This coordination to the CUS, pointing out to the accessible window to the cages of MIL-100(Fe), might lead to a decrease on its diameter, hindering the adsorption of EDOT moieties. In contrast, negligible interactions might occur with non-polar substances such as hexane, favoring the EDOT encapsulation.

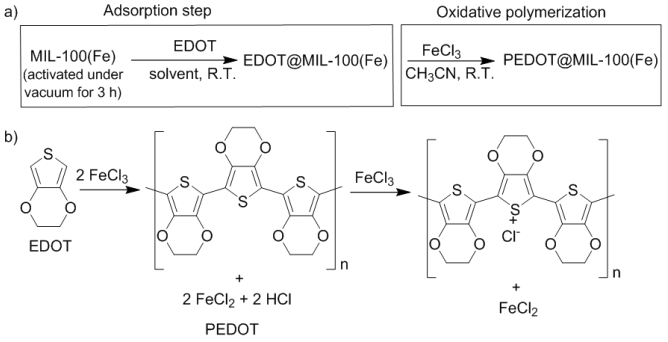

Figure 1. (a) Preparation procedure of PEDOT encapsulation inside the cavities of the MIL-100(Fe); (b) Illustration of the PEDOT formation and its partially oxidized polarons by $FeCl_3$.

Then, by selecting the hexane as impregnation solvent, the effect of the different EDOT:MOF wt. ratio (0.45:1, 0.9:1 and 1.8:1, corresponding to the denoted PEDOT@MIL-100(Fe)-1, 2 and 3 solids, respectively) on the encapsulation rate was assessed. These results evidence that the EDOT loadings increase with the initial EDOT concentration (40 ± 6 and 60 ± 9 PEDOT wt% for 45 and 90 PEDOT wt.%, respectively), reaching a plateau with a maximal value of around 70 wt.% for EDOT:MOF ratios higher than 0.9:1 (Figure S2 and Table 1). One has here to consider that the maximum EDOT loading, estimated by Monte-Carlo simulation at saturation, is *ca.* 70 wt.% (see experimental section for further details), confirming the small effect of the hexane on the encapsulation. The very good agreement between the experimental and theoretical loading suggests that a maximal PEDOT capacity was reached using this optimized encapsulation protocol (*i.e.* using a hexane solution EDOT:MOF wt. ratio of 0.9:1). According to this estimation based on Monte Carlo simulation, higher EDOT loadings than the maximum theoretical capacity might be explained by a location of the PEDOT moieties out from the MOF porosity (see below).

To further prove the location of the PEDOT moieties within the MOF pores, N_2 sorption isotherms were performed on the

Table 1. Textural properties, PEDOT content and ζ-potential values of PEDOT, MIL-100(Fe) and PEDOT@MIL-100(Fe) composites.

	S_{BET} ($m^2\ g^{-1}$)	Pore volume ($cm^3\ g^{-1}$)	EDOT: MIL100(Fe) (wt ratio)	PEDOT loading (wt %)	ζ-potential (mV)
MIL-100(Fe)	1210	0.54	-	-	-24 ±14
PEDOT@MIL-100(Fe)-1	800	0.35	0.45	40 ± 6	-1 ±13
PEDOT@MIL-100(Fe)-2	630	0.28	0.90	60 ± 9	35 ±15
PEDOT@MIL-100(Fe)-3	155	0.20	1.80	80 ± 12	37 ±12

initial MIL-100(Fe) and PEDOT@MIL-100(Fe) composites (Figure 2). The Brunauer-Emmett-Teller surface area (S_{BET}) and micropore volume significantly decrease when the polymer content increases (Table 1, Figure 2 a, b), in agreement with the location of the PEDOT inside the MIL-100(Fe) cages. In addition, the Horvath-Karazoe (HK) pore size distribution plot shows a shift of the pore sizes to lower values; the pore diameter at *ca.* 1.8 nm almost disappearing as a consequence of the PEDOT insertion (Figure 2a). The very low N_2 sorption capacity of the PEDOT@MIL-100(Fe)-3 composite could be related with the presence of a significant amount of PEDOT out of the pores and/or adsorbed on the outer surface of the crystals, blocking the N_2 access to the porosity.

In this line, the presence of an important PEDOT content on the outer surface of the MIL-100(Fe) was confirmed by determining the ζ-potential of the particles. While the starting MOF exhibits a negative surface charge (-24 mV), the ζ-potential values of the composites become neutral (-1 mV for PEDOT@MIL-100(Fe)-1) or positive (around +35 mV for both PEDOT@MIL-100(Fe)-2 and 3, respectively). This is in accordance with the presence of a positively charged polymer coating (free PEDOT ζ-potential = +32 ± 10mV) on the external surface of the MIL-100(Fe) particles. Therefore, the positive nature of the PEDOT may

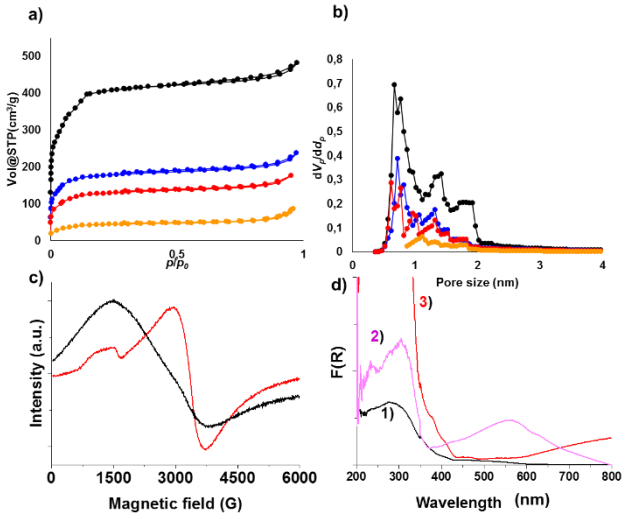

Figure 2. N_2 sorption isotherms at 77K (a) and Horvath-Kawazoe plots (b) of the MIL-100(Fe) (black) and PEDOT@MIL-100(Fe)-1, 2 and 3 composites (blue, red and yellow, respectively). c) EPR spectra of MIL-100(Fe) (1, black color) and PEDOT@MIL-100(Fe)-2 (2, red color). d) Diffuse reflectance UV-Vis spectra of MIL-100(Fe) (1), as-prepared PEDOT (2) and PEDOT@MIL100(Fe)-2 (3)

indicate the presence of hole polarons, generated during the oxidative polymerization. The hole polarons are here associated to positively charged sulfur in the aromatic ring of the PEDOT. Interestingly, the EPR spectrum of PEDOT@MIL-100(Fe)-2 was able to determine the presence of partially oxidized PEDOT polarons (Figure 2), thus providing a rationalization of the observed positive charge at PEDOT@MIL-100(Fe)-2 surface.[37] The presence of PEDOT within the MIL-100(Fe) solid was also assessed by diffuse reflectance UV-Vis spectroscopy (Figure 2). As already reported, the length of the polaron chain in polythiophenes is related with its UV-Vis absorption.[38] Thus, Figure 2 shows a broad visible absorption band extending beyond 800 nm that is attributed to the presence of PEDOT polarons. Note here the difference in the visible-near IR region between PEDOT and PEDOT@MIL-100(Fe)-2 (see figure 2d): free PEDOT shows a broad band centered at 550 nm that can be attributed to a short chain polaron, while the corresponding absorption band is shifted to near IR (~700 nm) in the PEDOT@MIL-100(Fe)-2, in agreement with a longer polaron absorption.

The structural integrity of MIL-100(Fe) in the PEDOT formation process was confirmed by PXRD before and after the PEDOT entrapment in the PEDOT@MIL-100(Fe)-1 and 2 composites, exhibiting the characteristic main reflections corresponding to the MIL-100(Fe) structure (Figure S4). Further, the decrease of the relative intensity of the first two Bragg peaks at 2θ values between 3 and 5 º is consistent with the filling of the pores by PEDOT chains. In the case of PEDOT@MIL-100(Fe)-3 composite, PXRD pattern shows an almost amorphous material with only a weak diffraction peak coming from the MIL-100(Fe) structure, probably due to the important amount of external amorphous PEDOT. This last result could also justify the absence of significant N_2 sorption. Finally, conductivity measurements were undertaken on the powdered samples, comparing the PEDOT polymer *ex situ* as prepared with the empty MIL-100(Fe)

Table 2. Electrical conductivity data of the materials

Sample	Conductivity ($S \cdot cm^{-1}$)*
PEDOT	$7.81 \cdot 10^{-4}$
MIL-100(Fe)	$8.09 \cdot 10^{-5}$
PEDOT@MIL-100(Fe)-1	$3.05 \cdot 10^{-3}$
PEDOT@MIL-100(Fe)-2	$7.51 \cdot 10^{-3}$
PEDOT@MIL-100(Fe)-3	$1.95 \cdot 10^{-3}$
PEDOT:PSS (Sigma-Aldrich)	$3.74 \cdot 10^{-3}$
*All calculations were carried out at 1 V Potential	

and the different PEDOT@MIL-100(Fe) composites. Table 2 summarizes the electrical properties of the different materials studied.

As expected, pristine MIL-100(Fe) pellets show lower conductivity compared with the PEDOT polymer, exhibiting a typical value around $8.09 \cdot 10^{-5}$ S·cm^{-1}. This conductivity is 10 times lower than that of *ex situ* free PEDOT polymer ($7.81 \cdot 10^{-4}$ S·cm^{-1}). Notably, the conductivity of the PEDOT@MIL-100(Fe) composites was in all cases much higher, with an optimal value for PEDOT@MIL-100(Fe)-2 that was 10 times higher than the free PEDOT as polymer reference. Higher amounts of PEDOT (*i.e.* PEDOT@MIL-100(Fe)-3) are associated with the presence of an important content of PEDOT out of the MOF porosity, being detrimental to the conductivity. Figure 3 shows the J-V curves of pristine MIL-100(Fe), the as-prepared PEDOT and a representative sample of PEDOT@MIL-100(Fe)-2. The higher conductivity of the composite could be explained by two reasons: first, by a polymer arrangement within the MOF porosity, induced by the polymer chains confinement inside the cages and/or second, a higher doping level of the occluded PEDOT, exhibiting higher polaron charge. This last could be supported by the larger amount of Cl^- anions remaining after the polymerization (Table S1), which would act as counter-anions compensating the positive charge of the sulfur polaron. As a hypothesis, the iron clusters of the MIL-100(Fe) structure, with an already proven redox activity,[35] could participate in the sulfur's oxidation in the polymer, leading to the formation of additional polarons.

In the literature, a higher conductivity value has been reported for PEDOT doped with polystyrene sulfonate (PEDOT:PSS), being this higher conductivity attributed to the alignment of the PSS doping chain.[39] Similar reasons (alignment of the PEDOT within the MOF porosity and higher number of polarons) could explain here the high conductivity of PEDOT@MIL-100(Fe)-2 in comparison with the *ex situ* polymerized PEDOT. Further, this hypothesis would be also supported by the differences in the UV-Vis spectra of PEDOT and PEDOT@MIL-100(Fe)-2, as previously discussed (Fig. 2d).

By further comparing our results with the previous reported PEDOT@MOF, our reached conductivity is slightly higher than the previously reported for the PEDOT entrapped within the chromium(III) terephthalate MIL-101(Cr) ($7.5 \cdot 10^{-3}$ *vs.* $1.1 \cdot 10^{-3}$ S·cm^{-1}).[28] This difference might be explained by the different nature of the employed polymer: Le Ouay and co-workers used I_2 as polymerizing and oxidizing agent instead of $FeCl_3$, and a non-redox Cr-based MOF matrix, which could lead to lower polaron density and thus, slightly lower conductivity.

Taking into account the above disclosed data, PEDOT@MIL-100(Fe)-2, which exhibits a good PEDOT insertion (60 wt%) within the MOF porosity and the highest conductivity value, was selected to carry out a deep structural and electrochemical characterization. It should be noted that the conductivity measurements prepared in this work have been carried out using pressed pellets of the different materials. Based on previous reports, it would be expected that the preparation of compact thin films with smooth and homogeneous structure facilitates the movement of charge carriers among the polymer chains and, therefore, the resulting conductivity values.[40]

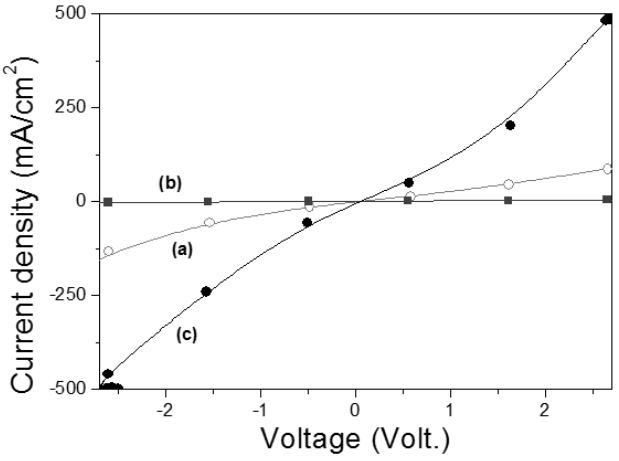

Figure 3. J-V plot corresponding to PEDOT (a), MIL-100(Fe) (b) and PEDOT@MIL-100(Fe)-2 (c).

Advanced structural characterization

To gain some insight about the accommodation of PEDOT in the MIL-100(Fe) cavities that could explain the high conductivity exhibited by this composite, a combined experimental (FTIR, XPS, PXRD and PDF analysis) and computational (Monte Carlo and DFT) approach was carried out (see experimental section). XPS analysis comparing Fe2p peak of fresh MIL-100(Fe) and PEDOT@MIL100(Fe)-2 shows in both cases the exclusive presence of Fe(III) in the same distribution of coordination spheres. Figures S5 and S6 show the experimental peaks for the different elements as well as the best deconvolution to individual components for MIL-100(Fe) and

Table 3. Main distances in simulated EDOT and PEDOT

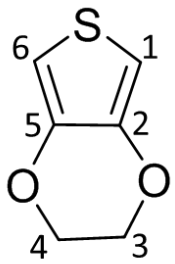

Distance (Å)	EDOT	PEDOT
C_1-C_2 C_2-C_5 C_2-O	1.4	1.4
S-C_1	1.8	1.8
C_1-C_5 C_2-C_3 C_2-C_4	2.5	2.5
S^+-Cl^-	-	2.8
S-Cl^-	-	3.6 & 4.5
S-O	3.8	3.8
S-C_3	4.8	4.8
PEDOT stacking	-	5.1

PEDOT@MIL100(Fe)-2, respectively. Of note the presence of Cl in the case of PEDOT-MIL-100(Fe)-2 that was absent in the MIL-100(Fe). Computational calculations should allow to attribute the experimental data to specific PEDOT conformations and interactions with other PEDOT chains of solid matrix. In addition, it allows also to determine the maximum PEDOT loading inside the MIL-100 voids. *Ex situ* PXRD patterns (Figure S7) were collected at the CRISTAL beamline (SOLEIL synchrotron source) by using glass capillaries filled with the EDOT, PEDOT, empty MIL-100(Fe), EDOT@MIL-100(Fe) and PEDOT@MIL-100(Fe)-2 (solids were previously dehydrated at 120ºC overnight; see experimental section).

First, PDF analysis was carried out on the isolated EDOT and PEDOT (Figure S8 and S9, see experimental details), comparing with the DFT simulated PDF obtained on the molecular models corresponding to the chemical formula given in the Molecular Simulation Section. This first step aims to generate a realistic configuration in order to identify and assign the main peaks corresponding to the main atomic distances observed in the conformation of the polymer (Table 2). Experimental and simulated PDF of the free EDOT moiety are in very good agreement, consistently assigning all the distances (Figure S8 and Table 3). PDF oscillations vanish after the longest S-C_3 distance in the molecule, indicating the absence of intermolecular structural correlations. For PEDOT, the PDF oscillations persist up to ~50 Å (Figure S9), which can be attributed to structural correlations along the polymeric chains. Although most of the short range atomic distances of PEDOT are similar to those ones in the EDOT (Figure S8 and Table 3), confirming the integrity of the monomeric units, some differences can nevertheless be observed after polymerization: i) a new intense peak appears at around 2.2 Å and may correspond to Fe-Cl distances ($R_{Fe\text{-}Cl}$~2.14),[41] associated with the presence of residual iron chloride, either as $FeCl_3$ (added for the polymerization) or in nodal positions. This hypothesis was further supported by the quantitative analysis of residual iron in the free PEDOT, despite the extensive washing (Table S1), and by the absence of this peak in the simulated PDF (not considering this impurity); ii) the intensity decrease for the peak corresponding to C_1-C_5, C_2-C_3, and C_2-C_4 could be explained by the higher electron density of the residual iron; iii) a shoulder at *ca.* 2.8 Å, which might correspond to the formation of an additional interaction between the S^+ and Cl^-, in concordance with the simulated distance (2.6-2.7 Å); iv) two additional intense broad peaks at *ca.* 3.6 and 4.5 Å might be also related with the distances between the chlorine and neutral sulfur from the neighbor monomers, in agreement with the simulated distances (3.3-3.9 and 4.6-4.8 Å; Figure S9); and v) the very broad peak at around 5.5 Å in the free EDOT seems to be shifted to a sharper peak at *ca.* 5.1 Å, which might correspond to the PEDOT stacking distances, as suggested by the DFT simulation with distances between 4.9 and 5.2 Å (Figure S9) and in agreement with a more fixed conformation.

Then, the pristine and EDOT or PEDOT encapsulated MIL-100(Fe) solids were compared. In order to obtain a more precise structural model of the MIL-100(Fe) framework, Rietveld refinement of the empty phase using synchrotron PXRD

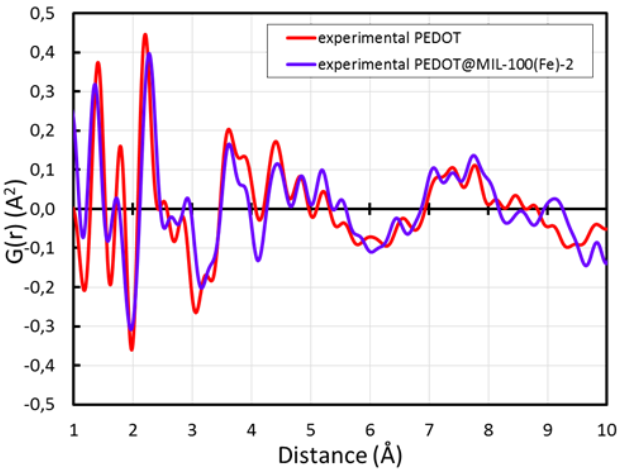

Figure 4. Subtracted PDF contribution of the PEDOT in the PEDOT@MIL-100(Fe)-2 compared with the free PEDOT and aromatic rings of the MOF and the PEDOT.

(CRISTAL beamline, SOLEIL) was initially undertaken, considering organic ligands as rigid bodies. The comparison of the unit cell parameter of the empty phase (a = 73.33(4) Å) with that of the PEDOT-containing MIL-100(Fe) (a = 73.04(4) Å) (decrease of about 0.4%), led us to assume that the MOF framework should not be strongly affected by the EDOT/PEDOT encapsulation. However, a clear peak broadening can be observed for the encapsulated compounds, which indicates a loss of structural coherence related to EDOT and PEDOT insertion. In order to extract the PDF of the encapsulated moieties, the differences between the PDFs of encapsulated and MIL-100(Fe) samples were computed. To take into account the effect of the change of coherence length, the PDFs were corrected by using a spherical envelope function and scaled before subtraction. When the differential PDF of the MIL-100(Fe) is further compared with that one of the PEDOT@MIL-100(Fe)-2 (Figure S10), only slight differences can be observed. This finding indicates that the MOF framework remains unaltered after PEDOT entrapment, allowing to subtract the MOF framework contribution to the EDOT@ and PEDOT@MIL-100(Fe)-2 samples in order to extract more precise information about the EDOT and PEDOT conformation inside the MIL-100(Fe) pores (Figure S11). Thus, on the whole, EDOT conformation at the free state and confined within the MIL-100(Fe) porosity is quite similar (Figure S11, top). However, an additional new peak at *ca.* 3.6 Å appears in the encapsulated EDOT, which might be associated to the formation of interactions between the EDOT molecule and the MIL-100(Fe) matrix, as further supported by the simulation, in which additional interactions are established between the carbon ($C_{1,6}$ and $C_{2,5}$) and oxygen atoms of the EDOT, and the aromatic ring and the carbon from the carboxylate group of the MOF, respectively. Additional hydrogen bonding interactions at around 2.8 Å are also evidenced by simulation, although not visible in the PDF analysis due to the negligible scattering power of hydrogen. In addition, the peak probability at around 5.5 Å might be due to some interactions between different EDOT molecules inside the MOF pores, as a consequence of the confinement effect. Other differences concern the slight

elongation of the 4.2 Å distance and the appearance of new distance probabilities at longer range (5-7 Å), consistent with the presence of inter-monomer interactions.

Finally, when comparing the conformation of the PEDOT free or encapsulated within the MIL-100(Fe) (Figure 4), one can also observe important similarities, indicating a related conformation. The long range oscillations of the PDF (Figure S11) appear to be quite similar, which indicates that the encapsulated PEDOT maintains a long range structural coherence, close to that in the free state. This is fully rational considering the high PEDOT content inside the mesoporous cavities (corresponding to 37 ± 6 and 58 ± 9 monomers *per* small and large cage, respectively; Table S1), which might lead to only a PEDOT fraction directly interacting with the pore wall and a second fraction interacting between them. However, some differences, as a consequence of the confinement effect, can be observed between the PEDOT@MIL-100(Fe)-2 and the free PEDOT. First, the distances corresponding to the first C-C neighbors (~1.4 Å) and S-C distance (~1.8 Å) are slightly contracted while the peaks at 2.2 and 2.5 Å are elongated, supporting a conformational change of the PEDOT heterocycles, in agreement with the polymer arrangement within the pores. Interestingly, the distance S^+ - Cl^- is initially longer (~2.8 *vs.* ~3.0 Å), which could partially explain the higher conductivity of the PEDOT@MIL-100(Fe)-2 composite. The modification of the relative intensity at around 3.7 Å (as well as slight changes at larger distances, ~5 and 8 Å) could be explained by the formation of polymer-matrix interactions, similarly to the EDOT@MIL-100(Fe) and in agreement with the molecular simulations. In particular, Monte Carlo simulations evidence weak interactions between the PEDOT-$C_{1,6}$ and the MOF-aromatic ring (3.8 Å), and the PEDOT-neutral sulfur and the oxygen from the carboxylate group of the MOF (3.5 Å), as well as between the PEDOT-oxygen atoms and the carbon from the carboxylate group of the MOF (3.7-3.8 Å), respectively. Keeping that in mind, in Monte Carlo simulations, the conformation of the PEDOT is not modified and can explain discrepancies between experimental and theoretical results. In this context, FTIR analysis confirms the presence of the PEDOT within the MOF by observing additional bands corresponding to the polymer (highlighted with * in Figure S12). Although difficult to assign due to the intrinsic disordered polymer characteristics, the presence of these bands provide experimental support of the formation of weak PEDOT-matrix interactions, as previously observed by PDF and molecular simulations. Thus, a shift to lower wavenumbers in the bands of the carboxylate group and trisubstituted aromatic ring of the trimesate ligand of the MOF (1650, 1460, 1370, 770 and 710 cm^{-1}), suggests the presence of weak interactions between the PEDOT and the carboxylate groups and aromatic rings of the MOF. On the whole, it is accepted that immobilization of different species within a porous matrix increases the stability of the guest by stablishing diverse host-guest interactions.[42–45] This called "confinement effect" is here observed: all these proposed PEDOT-MOF interactions ($C_{1,6}$-aromatic ring, S-O, O-C) lead to the confinement of the PEDOT inside the MIL-100(Fe) porosity, protecting the polymer and increasing its stability.

Electrochemical and electrochromic properties

The electrochemical behavior of the PEDOT and PEDOT@MIL-100(Fe)-2 composite deposited on fluorine doped tin oxide (FTO) conducting electrodes was investigated. Cyclic voltammetry studies were initially performed to evaluate the electrochemical stability of the PEDOT and PEDOT@MIL-100(Fe)-2. Figure 5 shows the cyclic voltammograms after 50 cycles using $LiClO_4$ and acetonitrile as electrolyte. The shape of the curves is very similar, exhibiting the characteristic oxidation and reduction peaks at about 0.6 and -0.6 Volt, respectively. However, a decrease of 30% of the current with respect to the initially measured current is observed in the case of the free PEDOT polymer (Figure 5). In the case of the PEDOT-containing MOF, the reduction and oxidation current diminishes about 10%, indicating that the structure of the MOF provides a substantial protective effect to the intrinsically instable PEDOT. We also studied the electrochromic properties of PEDOT and PEDOT@MIL-100(Fe)-2 samples deposited by screen printing on transparent conducting FTO electrodes. First of all, we measured the absorption changes in the absorption spectra upon electrochemical oxidation/reduction conditions. Figure 6 shows the absorption spectra of the films, which were obtained by applying a constant potential of + 1 V for oxidation and -1 V for reduction. Oxidation of the polymer shows a decrease in the absorbance throughout the visible region since the color changes from a dark blue absorbing state (reduced form) to a sky blue (oxidized form). Also, we observe different absorbance maxima in the absorbing state with values of 600 and 550 nm for the PEDOT and PEDOT@MIL-100(Fe)-2, respectively. On the other hand, the optical switching properties of these materials were evaluated by repeated potential steps between their reduced and oxidized states. In these studies, the variation of the absorption of the material films was monitored as a function of time at a constant wavelength (600 nm). As depicted in Figure 6, the evolution of the optical absorption changes demonstrates a good switching behavior of the PEDOT@MIL-100(Fe)-2 composite. These experiments conclusively show that PEDOT@MIL-100(Fe)-2 composite exhibits a better electrochromic behavior than the reference, free PEDOT polymer, since after 20 cycles the changes of the absorbance were practically negligible.

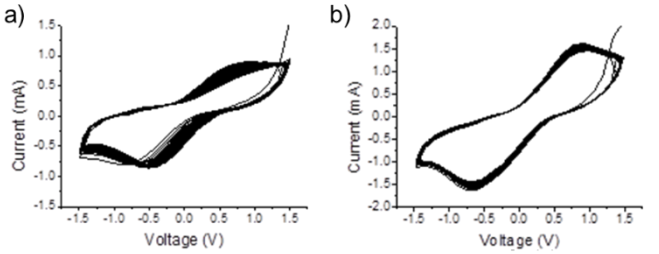

Sample	% Current at E_{red} (Volt.)	% Current at E_{ox} (Volt.)
***Ex-situ* PEDOT**	28.8 ± 0.5	30.2 ± 0.5
PEDOT@MIL-100(Fe)-2	11.2 ± 0.5	10.3 ± 0.5

Figure 5. Top: Cyclic voltammetry of layers of PEDOT (a) and PEDOT@MIL-100(Fe)-2 (b) after 50 cycles between 1.5 to -1.5 Volt at 100 mVs^{-1} scan rate. Bottom: Main electrochemical parameters of PEDOT and PEDOT@MIL-100-2 after 50 or 20 cycles

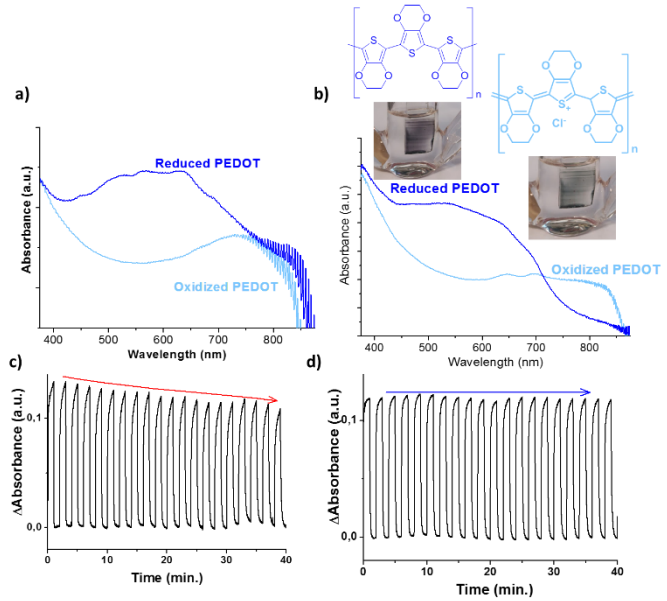

Figure 6. UV-Vis spectroelectrochemistry for PEDOT (a) and PEDOT@MIL-100(Fe)-2 (b) deposited films on FTO showing their reduced and oxidized states. Electrochromic switching monitoring the optical absorbance changes at 600 nm of PEDOT (c) and PEDOT@MIL-100(Fe)-2 (d) acquired by repeated potential steps between -1 V (reduced) and 1 V (oxidized) in 0.1 M $LiClO_4$ and acetonitrile.

However, in the case of the free PEDOT, a decrease about 20 % in the response after the same number of cycles was observed. Therefore, these results are consistent with the previous voltammetry studies, confirming a higher stability in the case of the PEDOT@MIL-100(Fe)-2 composite.

Furthermore, the stability of the films employed for the cyclic voltammetries or for the electrochromic measurements was evaluated by PXRD and SEM-EDX, focused ion beam SEM (FIB-SEM) and atomic force microscopy (AFM) measurements. PXRD patterns show that, in both cases, the characteristic diffraction peaks of the PEDOT@MIL-100(Fe)-2 solid after 50 or 20 cycles for the voltammetric or electrochromic. measurements, respectively (Figure S13). The poor intensity observed in the fresh and cycled films used for the electrochromic measurements is due to the low amount of composite deposited in the FTO support.

SEM-EDX images, collected in two perspectives (flat surface and cross-section; see Figures S14 and S15), show a surface with a homogeneously distributed material before and after the voltammetric or electrochromic measurements, evidencing a good stability and adhesion of the composite films to the support. The spatial distribution of the elements in the composite film, evaluated by EDX mapping analysis, also evidences a regular distribution of the MOF solid (see Fe, C and O) and the PEDOT (see S, Cl, C and O) both at the surface and through the cross-section before and after voltammetric or electrochromic evaluation. Note that the presence of F, Sn and Si corresponds to the FTO composition. Finally, FIB-SEM (Figure S16) and AFM (Figure S17) images of the initial PEDOT@MIL-100(Fe)-2 film show a ~730 nm-thickness homogeneous layer with a roughness ~300 nm. After cyclic voltammetry (50 cycles), the films present an unaltered thickness with a slight increase of the roughness (~ 350 nm), confirming the stability of the sample (Figure S16-17). These observations support the good cyclability of the composite upon both measurements.

Conclusions

The highly conducting polymer PEDOT was successfully entrapped (reaching remarkable capacities; 60 wt%) within the benchmarked nontoxic MIL-100(Fe) mesoporosity using an efficient and simple two-step process: by initially encapsulating the EDOT monomer followed by its in situ oxidative polymerization within the MOF pores. The resulting PEDOT@MIL-100(Fe) composite exhibits an electrical conductivity 10 times higher than the free polymer, as a consequence of the nanoarrangement of the PEDOT inside the MOF, associated to a larger interatomic distance between the S^+ and the Cl^- in the polymer. Remarkably, this stable composite presents interesting electrochemical and electrochromic properties derived from the polymer with, however, enhanced cyclability and optical switching due to a protective effect of the MOF matrix. These results pave the way for the development of novel robust optoelectronic polymer-MOF devices and their application in cutting-edge technological areas (*e.g.* energy efficient buildings, solar energy, reflecting surfaces).

Experimental section

Synthetic procedures:

Materials: All the reagents and solvents used in this work were of analytical grade (excepting the anhydrous acetonitrile which was HPLC grade) and supplied by Sigma-Aldrich.

PEDOT: PEDOT was prepared following previously reported procedures.[46] Briefly, an acetonitrile solution of EDOT (135 µL, 1.267 mmol) was introduced in a Schlenk tube and purged with N_2 for 15 min. The oxidative polymerization of EDOT was carried out by the addition of a solution of anhydrous $FeCl_3$ (2.877 mmol *per* 1.267 mmol of EDOT) in anhydrous acetonitrile under inert atmosphere. After 18 h under stirring, the obtained dark-blue solid was washed with acetonitrile, distilled water and ethanol. Finally, the solid was dried in an oven at 100 °C for 24 h.

MIL-100(Fe): MIL-100(Fe) ($Fe_3O(OH)(H_2O)_2(C_9H_3O_6)_2$) was synthetized according to reported procedures.[47] Briefly, the corresponding amounts of triethyl 1,3,5-benzenetricarboxylate (6.6 mmol; lab prepared, see below) and $FeCl_3{\cdot}6H_2O$ (10 mmol) were added to a Teflon-lined autoclave (125 mL) together with 50 mL of distilled water. The autoclave was heated at 130 °C from room temperature (RT) in 1 h and then, maintained at this temperature for 72 h. After cooling to RT, the obtained orange material was filtered, recovered and dried in an oven at 100 °C overnight.

The as-synthesized MIL-100(Fe) solid was first washed in 150 mL of milliQ water *per* gram for 3 h under reflux and then, with 150 mL *per* gram of absolute ethanol for 3 h under reflux. Then, it was suspended in a 0.1 M KF solution (50 mL *per* gram of product) at 70 °C for 3h. The last washing step consisted on a

suspension of the solid in milliQ water (150 mL *per* gram) at RT for 2 h. Finally, the solid was dried in an oven at 100 °C for 24 h.

Triethyl-1,3,5-benzenetricarboxylate: The ester derivate of the MIL-100 linker was prepared adding 5 g of trimesic acid in 100 mL of absolute ethanol with 2 mL of H_2SO_4 (98%) in a 250 mL round bottom flask at 90 °C for 24 h. After cooling to RT, a white solid was filtered, washed with diethyl ether and dried at 80 °C overnight.

EDOT encapsulation in MIL-100(Fe): 200 mg of the previously dehydrated MIL-100(Fe) (dried at 100 °C for 24 h) were introduced in a 50 mL-Schlenk tube. The system was heated at 150 °C under vacuum for 3 h to remove the adsorbed water in the solid. After cooling-down at RT, the required amount of monomer (45, 90 or 180 in wt% with respect to the MIL-100(Fe)), previously dissolved in acetonitrile or hexane and purged with N_2, was added to the Schlenk tube. The system was magnetically stirred for 4 h under N_2. Then, the suspension was filtered, reintroducing the solid (EDOT@MIL-100(Fe)) in a Schlenk tube for the following polymerization.

PEDOT polymerization in the MIL-100(Fe): The Schlenk tube containing the EDOT@MIL-100(Fe) solid was submitted to two vacuum/N_2 cycles at RT. Then, a previously N_2-purged solution of anhydrous $FeCl_3$ in anhydrous acetonitrile was added. After 16 h of reaction under stirring in N_2 atmosphere, the resulting material was washed thoroughly with acetonitrile, water and ethanol. Finally, the solid was dried at 100 °C for 24 h.

Characterization:

High-resolution synchrotron powder diffraction experiments were carried out at the CRISTAL beamline, SOLEIL Synchrotron (Gif-sur-Yvette, France). A monochromatic beam was extracted from the U20 undulator beam by means of a Si(111) double mono-chromator. Its wavelength of 0.51368 Å was refined from a LaB_6 (NIST Standard Reference Material 660a) powder diagram recorded just before the experiment. High angular resolution in the diffracted beam is obtained with a 21-perfect crystals Si (111) multi-analyzer. The sample was loaded in a 0.7 mm capillary (Borokapillaren, GLAS, Schönwalde, Germany), dehydrated at 120 °C overnight and sealed. Then, the capillary was mounted on a spinner rotating at about 5 Hz to improve particle averaging. Diffraction data were collected in less than 4 h in continuous scanning mode and the diffractogram was obtained from the precise superposition and addition of the 21 channels data. The Rietveld refinements of the powder X-ray diffraction (PXRD) patterns were carried out using the Topas program (Topas V5: General Profile and Structure Analysis Software for Powder Diffraction Data, Bruker AXS Ltd. 2008).

For Pair Distribution Function (PDF) analysis, the data were collected on the same samples and at the same energy, but in order to improve counting statistics and maximum $Q=4\pi.sin\vartheta/\lambda$, a XPAD3.2 hybrid pixel 2D detector was used. Diffraction images were collected every degree from 0 to 120° 2θ, with a 10 s exposure time. This procedure was repeated up to 8 times for a total of 2.7 h. The images were then corrected, integrated and summed to yield 1D powder diffraction patterns with Q_{max} = 20 $Å^{-1}$ using the software ImageReducerCristal developed at SOLEIL. Similar data were also collected for an empty capillary and Nickel and LaB_6 standard samples for background subtraction and determination of the instrument resolution function. The PDFs were obtained with the PDFGetX3 software.[48] As an example of the data quality, the fit of the PDF for the Ni standard sample up to 50 Å using PDFGUI[49] is shown in the SI (Figure S18).

PXRD routine patterns were collected using a D8 Advance Bruker diffractometer with Cu Kα1 radiation (λ = 1.54056 Å) from 3 to 25° (2θ) using a step size of 0.02° and 2.5 s *per* step in continuous mode. Nitrogen sorption isotherms were collected at 77 K using a BEL sorp Mini (Bel, Japan). Prior to the analysis the samples were activated at 130 °C under primary vacuum for 3 h. Fourier transformed infrared (FTIR) spectra were collected in the 4000 to 400 cm^{-1} range using a Thermo Nicolet 6700 FTIR with ATR accessory instrument (Thermo scientific, USA). Thermogravimetric measurements (TGA) were performed on a Perkin Elmer Diamond TGA/DTA STA 6000 in the 25 -600 °C range under at 5 °C/min and an O_2 flow of 20 mL min^{-1}. Fe content was quantified using an induced coupled plasma atomic emission spectrometer (ICP-OES) 2300 DV from Perkin Elmer. Elemental analyses were carried out in a Flash 2000 analyzer from Thermo Scientific. ζ-potential values of PEDOT, MIL-100(Fe) and PEDOT@MIL-100(Fe) suspensions in Milli-Q water (10 mg L^{-1}) were measured using a Malvern Zetasizer instrument (Nano series). Morphology and microanalyses of the samples were analyzed using a scanning electron microscope (SEM) coupled with a EDX detector (Oxford instrument and Hitachi TM-1000) and coupled to a FIB instrument. The thickness and roughness of the MOF films were measured using an AFM instrument working in contact mode in air at ambient temperature using a Veeco apparatus operating in tapping mode. Electron paramagnetic resonance (EPR) spectra of solid samples previously degassed were recorded on a Bruker EMX spectrometer working at 9.803 GHz, sweep width 3489.9 G, time constant 40.95 ms, modulation frequency 100 kHz, modulation width 1 G, microwave power 19.92 mW. Diffuse reflectance UV-Vis measurements were recorded in a Perkin Elmer (Lambda 19) equipped with an integrating sphere. Remarkably, PEDOT@MIL-100(Fe) films were stable for > 6 months stored under ambient conditions (relative humidity ~ 55%, 20ºC, atmospheric conditions and unprotected from light). X-ray photoelectron spectroscopy (XPS) measurements were carried out on a SPECS spectrometer equipped with an MCD-9 detector using a monochromatic Al X-ray source (Kα= 1486.6 eV). CASA software has been used for spectra deconvolution setting at 284.4 eV the C1s peak as reference.

Molecular simulations:

Density Functional Theory (DFT) calculations have been performed to elucidate the intrinsic conformation of the two molecules EDOT and PEDOT. For that purpose, a geometry-optimization has been performed on molecular models using DMol³ software and the PBE GGA density functional combined with double numerical basis set containing polarization functions on hydrogen atoms (DNP).[50] In addition, all electrons have been taken into account. The comparison of the results with DFT calculations considering the Grimme method for DFT-

D shows no difference. The convergence criteria for energy (10^{-5} Ha), maximal force (0.002 Ha/Å) and maximal displacement (0.005 Å) allows the calculations to reach the global minimum and propose the plausible conformations of the molecules. In the case of PEDOT, two models have been tested: a simple structure ($C_{18}H_{14}O_6S_3Cl$) and a double structure in order to estimate the impact of long distance modifications. In addition, two kind of configurations (see Figure S19) have also been compared regarding the organization of the cycles one to another. From the DFT calculations, it follows that the conformation corresponding to the Figure S17b is the most stable. Furthermore, a calculation on a stacking of two EDOTs or PEDOTs has also been performed to estimate the interaction distance between neighbor polymer units.

Using such calculations, it is therefore possible to extract the partial charges using the ESP method for both EDOT and PEDOT (see SI for partial charges for the molecular models; Figure S19). In complement to the DFT calculations, Grand Canonical Monte Carlo (GCMC) simulations using SORPTION software have been performed to estimate the maximal amount adsorbed in the MIL-100(Fe) structure and to evaluate the main interaction existing between the EDOT/PEDOT and the MIL-100(Fe) framework, which is impossible by DFT calculations due to the size of the unit cell of the MOF. For that purpose, a simulation box containing the MIL-100(Fe) structure model (see Figure S20) issued from the literature has been used.[32] The pristine MIL-100 model considered in this study was obtained from the reported structure optimized using classical force field combining partial charges and Lennard-Jones parameters. ESP charges calculated previously by DFT for EDOT/PEDOT are combined with charges issued from equalization electronegativity method[51] for MIL-100(Fe) (calculated using Materials Studio) to evaluate the electrostatic interaction. For the van der Waals interaction, Universal Force Field (UFF) has been used for the 12-6 Lennard Jones (LJ) atomic parameters.[52] LJ interatomic potential has thus been calculated using the Lorentz-Berthelot combining rule with a cut-off radius equal to 12 Å. In contrast, the long range electrostatic interactions were calculated using the Ewald summation technique.

In order to probe the confinement of the EDOT/PEDOT molecules, their insertion was investigated by Grand Canonical Monte Carlo simulations. GCMC calculations have been performed at 300 K with typically 5 millions of Monte Carlo steps for equilibration and 1 million steps for production. From these calculations, the plausible configurations of the EDOT/PEDOT molecules adsorbed on the pores surfaces of the MIL-100(Fe) framework can be determined as well as the main interactions governing the adsorption of these molecules.

Note here that, by validating computing simulations with experimental data provided by PDF analysis and IR, allow to identify interatomic distances and provide relevant information of PEDOT conformation and host-guest interactions at the atomic level.

Conductivity measurements:

All the conductivity measurements were performed in a home-made system using a sourcemeter Keithley 2601 connected with a PC using LabTracer software that controls the scan and also provides data storage capability. The sourcemeter was previously calibrated by using a copper foil as a standard. A detailed schematic description of the equipment has been previously published.[53] Briefly, 20 mg of each powdered sample were placed in a sample holder of 13 mm diameter between two polished steel pellets that allows pressurizing during the measurements. The samples were pressed at 8 Ton·cm^{-2} with a pneumatic press piston and the electrical conductivity was measured between the top and bottom metallic surface of the press holder at 25°C. For the sake of comparison, commercial PEDOT:PSS (Aldrich 483095-250G) was characterized upon the same conditions by drying and grinding in powder. Thickness of the pressed samples was measured by using a Mitutoyo instrument with an accuracy of ± 0.0001 in 2 µm.

Electrical resistivity of the materials was calculated by using the equation 1 and using the resistance (**R**) calculated at 1 V with the dimensions of the pressed pellet, the thickness is the length and the area was calculated from the diameter of the conductive pellet.

$$\rho = R \cdot a / l \qquad \text{Eq. 1}$$

where R is the resistance, l the thickness and a the area of the circular pellet (13 mm diameter).

Since the electrical conductivity is the reciprocal of the resistivity, was calculated by taking the inverse of resistivity ($\sigma=1/\rho$).

Electrochemical and electrochromic experiments:

The electrochemical experiments were performed using an AMEL 7050 potentiostate. A fluorine-doped tin oxide (FTO) substrate coated by screen-printing with a paste of the material (10 wt.% in terpineol) was used as working electrode. Electrochromic experiments were carried out in a 0.1 M lithium perchlorate solution in acetonitrile and using a three-electrode configuration with a platinum wire as the counter electrode and saturated Ag/AgCl as the reference electrode. A home-made quartz electrochemical cell mounted in a VARIAN CARY 300 SCAN UV-Vis spectrophotometer was used for monitoring the absorption changes upon bias potential application. For the changes in the absorption spectrum scans from +1 to -1 V were carried out. For the electrochromic switching, the spectrophotometer was fixed at 600 nm and sequential cycles applying voltages of +1 and -1 Volt with a duration of 60 s for recording color changes. Note that all the experiments were performed under ambient conditions (under air and moisture) and using non anhydrous AcN, supporting the stability of the PEDOT@MIL-100(Fe) films under moisture.".

Conflicts of interest

There are no conflicts to declare.

Acknowledgements

This work was supported by a 2017 Leonardo Grant for Researchers and Cultural Creators, BBVA Foundation. The work

was also partially supported by IMDEA Energy and Raphuel project (ENE2016-79608-C2-1-R, MINECOAEI/FEDER, UE). PH acknowledges the Spanish Ramón y Cajal Programme (grant agreement no. 2014-16823). S.N. thanks the Spanish Ministerio de Educación, Cultura y Deporte for José Castillejo mobility programme (CAS14/00067) and financial support by Fundación Ramón Areces (XVIII Concurso Nacional para la Adjudicación de Ayudas a la Investigación en Ciencias de la Vida y de la Materia, 2016). We also thank the synchrotron Soleil from providing access to the Cristal beamline.

Notes and references

1 P. M. S. Monk, R. J. Mortimer and D. R. Rosseinsky, *Electrochromism : fundamentals and applications*, VCH, 1995.

2 V. V. Kondalkar, R. R. Kharade, S. S. Mali, R. M. Mane, P. B. Patil, P. S. Patil, S. Choudhury and P. N. Bhosale, *Superlattices Microstruct.*, 2014, **73**, 290–295.

3 C. E. Patil, N. L. Tarwal, P. R. Jadhav, P. S. Shinde, H. P. Deshmukh, M. M. Karanjkar, A. V. Moholkar, M. G. Gang, J. H. Kim and P. S. Patil, *Curr. Appl. Phys.*, 2014, **14**, 389–395.

4 A. Benoit, I. Paramasivam, Y. C. Nah, P. Roy and P. Schmuki, *Electrochem. commun.*, 2009, **11**, 728–732.

5 R. J. Mortimer, *J. Electrochem. Soc.*, 1991, **138**, 633–634.

6 R. J. Mortimer, A. L. Dyer and J. R. Reynolds, *Displays*, 2006, **27**, 2–18.

7 T. Abidin, Q. Zhang, K.-L. Wang and D.-J. Liaw, *Polymer*, 2014, **55**, 5293–5304.

8 T. K. Das and S. Prusty, *Polym. Plast. Technol. Eng.*, 2012, **51**, 1487–1500.

9 T. Bein and P. Enzel, *Angew. Chemie - Int. Ed.*, 1989, **28**, 1692–1694.

10 C.-G. Wu and T. Bein, *Science*, 1994, **264**, 1757–1759.

11 A. Thomas, F. Goettmann and M. Antonietti, *Chem. Mater.*, 2008, **20**, 738–755.

12 T. Uemura, Y. Kadowaki, N. Yanai and S. Kitagawa, *Chem. Mater.*, 2009, **21**, 4096–4098.

13 G. Ferey, C. Mellot-Draznieks, C. Serre, F. Millange, J. Dutour, S. Surblé and I. Margiolaki, *Science*, 2005, **309**, 2040–2042.

14 H. Furukawa, N. Ko, Y. B. Go, N. Aratani, S. B. Choi, E. Choi, A. O. Yazaydin, R. Q. Snurr, M. O'Keeffe, J. Kim and O. M. Yaghi, *Science*, 2010, **329**, 424–428.

15 O. K. Farha, I. Eryazici, N. C. Jeong, B. G. Hauser, C. E. Wilmer, A. A. Sarjeant, R. Q. Snurr, S. T. Nguyen, A. Ö. Yazaydın and J. T. Hupp, *J. Am. Chem. Soc.*, 2012, **134**, 15016–15021.

16 Themed issues: *Chem. Soc. Rev., 2009, 1201; Chem. Rev., 2012, 112; Chem. Soc. Rev., 2014, 5415.*

17 M. P. Suh, H. J. Park, T. K. Prasad and D.-W. Lim, *Chem. Rev.*, 2011, **112**, 782–835.

18 M. R. Ryder and J.-C. Tan, *Mater. Sci. Technol.*, 2014, **30**, 1598–1612.

19 C. R. Wade, M. Li and M. Dincă, *Angew. Chemie - Int. Ed.*, 2013, **52**, 13377–13381.

20 C.-W. Kung, T. C. Wang, J. E. Mondloch, D. Fairen-Jimenez, D. M. Gardner, W. Bury, J. M. Klingsporn, J. C. Barnes, R. Van Duyne, J. F. Stoddart, M. R. Wasielewski, O. K. Farha and J. T. Hupp, *Chem. Mater.*, 2013, **25**, 5012–5017.

21 Y. X. Xie, W. N. Zhao, G. C. Li, P. F. Liu and L. Han, *Inorg. Chem.*, 2016, **55**, 549–551.

22 K. AlKaabi, C. R. Wade and M. Dincă, *Chem*, 2016, **1**, 264–272.

23 I. Mjejri, C. M. Doherty, M. Rubio-Martinez, G. L. Drisko and A. Rougier, *ACS Appl. Mater. Interfaces*, 2017, **9**, 39930–39934.

24 T. Uemura, N. Uchida, A. Asano, A. Saeki, S. Seki, M. Tsujimoto, S. Isoda and S. Kitagawa, *J. Am. Chem. Soc.*, 2012, **134**, 8360–8363.

25 C. Lu, T. Ben, S. Xu and S. Qiu, *Angew. Chemie - Int. Ed.*, 2014, **53**, 6454–6458.

26 T. Kitao, S. Bracco, A. Comotti, P. Sozzani, M. Naito, S. Seki, T. Uemura and S. Kitagawa, *J. Am. Chem. Soc.*, 2015, **137**, 5231–5238.

27 M. W. A. MacLean, T. Kitao, T. Suga, M. Mizuno, S. Seki, T. Uemura and S. Kitagawa, *Angew. Chemie - Int. Ed.*, 2016, **55**, 708–713.

28 B. Le Ouay, M. Boudot, T. Kitao, T. Yanagida, S. Kitagawa and T. Uemura, *J. Am. Chem. Soc.*, 2016, **138**, 10088–10091.

29 T. Wang, M. Farajollahi, S. Henke, T. Zhu, S. R. Bajpe, S. Sun, J. S. Barnard, J. S. Lee, J. D. W. Madden, A. K. Cheetham and S. K. Smoukov, *Mater. Horizons*, 2017, **4**, 64–71.

30 J. Kawahara, P. A. Ersman, I. Engquist and M. Berggren, *Org. Electron. physics, Mater. Appl.*, 2012, **13**, 469–474.

31 M. F. Zainal and Y. Mohd, *Polym. - Plast. Technol. Eng.*, 2015, **54**, 276–281.

32 P. Horcajada, S. Surblé, C. Serre, D. Y. Hong, Y. K. Seo, J. S. Chang, J. M. Grenèche, I. Margiolaki and G. Férey, *Chem. Commun.*, 2007, **100**, 2820–2822.

33 Y.-K. Seo, J. W. Yoon, J. S. Lee, U.-H. Lee, Y. K. Hwang, C.-H. Jun, P. Horcajada, C. Serre and J.-S. Chang, *Microporous Mesoporous Mater.*, 2012, **157**, 137–145.

34 A. Dhakshinamoorthy, M. Alvaro, P. Horcajada, E. Gibson, M. Vishnuvarthan, A. Vimont, J.-M. Grenèche, C. Serre, M. Daturi and H. Garcia, *ACS Catal.*, 2012, **2**, 2060–2065.

35 J. W. Yoon, Y.-K. Seo, Y. K. Hwang, J.-S. Chang, H. Leclerc, S. Wuttke, P. Bazin, A. Vimont, M. Daturi, E. Bloch, P. L. Llewellyn, C. Serre, P. Horcajada, J.-M. Grenèche, A. E. Rodrigues and G. Férey, *Angew. Chemie Int. Ed.*, 2010, **49**, 5949–5952.

36 J. Xu, H. S. O. Chan, C. C. Ng and T.-S. Chung, *Synth. Met.*, 2002, **132**, 63–69.

37 W. Domagala, B. Pilawa and M. Lapkowski, *Electrochim. Acta*, 2008, **53**, 4580–4590.

38 J. V. Caspar, V. Ramamurthy and D. R. Corbin, *J. Am. Chem. Soc.*, 1991, **113**, 600–610.

39 B. J. Worfolk, S. C. Andrews, S. Park, J. Reinspach, N. Liu, M. F. Toney, S. C. B. Mannsfeld and Z. Bao, *Proc. Natl. Acad. Sci.*, 2015, **112**, 14138–14143.

40 C. Liu, F. Jiang, M. Huang, R. Yue, B. Lu, J. Xu and G. Liu, *J. Electron. Mater.*, 2011, **40**, 648–651.

41 R. Bach, S. David, H. Bernhard Schlegel and C. J. Nagel, *J. Phys. Chem.*, 1996, **100**, 8770–8776.

42 M. B. Majewski, A. J. Howarth, P. Li, M. R. Wasielewski, J. T. Hupp and O. K. Farha, *CrystEngComm*, 2017, **19**, 4082–4091.

43 J. Aguilera-Sigalat and D. Bradshaw, *Coord. Chem. Rev.*, 2016, **307**, 267–291.

44 R. Semino, J. C. Moreton, N. A. Ramsahye, S. M. Cohen and G. Maurin, *Chem. Sci.*, 2018, **9**, 315–324.

45 S. Rojas, I. Colinet, D. Cunha, T. Hidalgo, F. Salles, C. Serre, N. Guillou and P. Horcajada, *ACS Omega*, 2018, **3**, 2994–3003.

46 R. Corradi and S. P. Armes, *Synth. Met.*, 1997, **84**, 453–454.

47 R. Canioni, C. Roch-Marchal, F. Sécheresse, P. Horcajada, C. Serre, M. Hardi-Dan, G. Férey, J.-M. Grenèche, F. Lefebvre, J.-S. Chang, Y.-K. Hwang, O. Lebedev, S. Turner and G. Van Tendeloo, *J. Mater. Chem.*, 2011, **21**, 1226–1233.

48 P. Juhás, T. Davis, C. L. Farrow, S. J. L. Billinge and IUCr, *J. Appl. Crystallogr.*, 2013, **46**, 560–566.

49 C. L. Farrow, P. Juhas, J. W. Liu, D. Bryndin, E. S. Božin, J. Bloch, T. Proffen and S. J. L. Billinge, *J. Phys. Condens. Matter*, 2007, **19**, 335219.

50 J. P. Perdew, K. Burke and M. Ernzerhof, *Phys. Rev. Lett.*, 1996, **77**, 3865–3868.

51 A. K. Rappe and W. A. Goddard, *J. Phys. Chem.*, 1991, **95**, 3358–3363.

52 A. K. Rappe, C. J. Casewit, K. S. Colwell, W. A. Goddard and W. M. Skiff, *J. Am. Chem. Soc.*, 1992, **114**, 10024–10035.

53 M. Álvaro, J. F. Cabeza, D. Fabuel, H. García, E. Guijarro and J. L. Martínez de Juan, *Chem. Mater.*, 2006, **18**, 26–33.